HF Radar Data Assimilation in the Monterey Bay Area

Jeffrey D. Paduan
Naval Postgraduate School
Monterey, California

Igor Shulman
Naval Research Laboratory
Stennis Space Center, Mississippi

Version Date: 5 May 2003

ABSTRACT

The utility of High Frequency (HF) radar data for improving numerical circulation model predictions is evaluated. Comparisons of the statistical properties of the (CODAR-type) HF radar data and the observed wind indicate a strong correlation between the dominant alongshore, upwelling-favoring wind forcing and HF radar-derived surface currents along the central California coastline. Because inadequate knowledge of the wind stress is probably a significant source of error in the model solutions, the idea of using HF radar data to provide corrections to the model wind forcing is promising. Different HF radar data assimilation schemes are compared and judged based on the correlations observed between model currents and independent observations from two mooring sites. Analysis of correlation maps between model-predicted and observed currents indicates a spatial and temporal shift between modeled and observed features. However, the impact of HF radar data assimilation reduces these spatial and temporal shifts. A significant improvement in the correlation between the model and observed subsurface currents is achieved when an Ekman-layer projection of the corrections is included. In this approach, assimilation of HF radar data produces additional Ekman pumping (vertical velocity) based on the horizontal pattern of model-observed velocity mismatch at the surface.

1. Introduction

The coastal ocean represents one of the most critical marine provinces in terms of recreation, mineral exploitation, short-term weather forecasting, and national security. The coastal areas, including the continental shelves, are also home to the majority of marine species considered important economically or as indicators of anthropogenic impacts on the marine ecosystem. Despite these varied interests, observing and modeling the coastal ocean are still difficult and poorly achieved tasks. Like in all ocean areas, maintaining instruments in situ is difficult and

expensive. From the modeling perspective, the need for very high resolution and the preponderance of open boundaries present extreme challenges to realistic simulations.

In recent years an evolving capability to use shore-based, high frequency (HF) radar systems to continuously monitor vast stretches of coastal ocean surface currents has presented one new possibility for improving our understanding and monitoring capabilities in these marine systems (Paduan and Graber, 1997). HF radar networks exploit radiowave backscatter in the frequency band from 3-30 Mhz to map ocean surface currents. Most systems operate in the range of 12-25 MHz and produce maps out to ranges reaching 60 km from shore with horizontal resolutions of 1–3 km (e.g., Paduan and Rosenfeld, 1996; Graber et al., 1997). At lower frequencies near 5 MHz, ranges of 200 km are possible using shore-based systems but with decreased horizontal resolution of 5-10 km (Barrick, 2003).

Monterey Bay has been the site of HF radar measurements for a number of years, particularly measurements made using CODAR/SeaSonde-type instruments. Surface ocean velocity data from these systems have been described in previous settings (e.g., Paduan and Rosenfeld, 1996; Paduan and Cook, 1997; Lipphardt et al., 2000). During the period 1999-2000, particular effort was paid to collecting continuous HF radar-derived current maps from three sites surrounding Monterey Bay as part of the National Ocean Partnership Program project entitled "an Innovative Coastal-Ocean Observing Network (ICON)." The project also involved the deployment and maintenance of four deep-ocean mooring sites and the development of a nested, high-resolution ocean circulation model, among other activities (Paduan et al., 1999). The locations of Monterey Bay, the three SeaSonde sites surrounding it, and the two primary mooring sites used in this study are shown in Figure 1.

In recent years, the utility of HF radar-derived surface velocity fields as input to data-assimilating numerical circulation models has been the focus of several studies. It is also the primary focus of this study. The potential benefits of HF radar data are large, particularly in light of the dearth of real-time observations from the marine environment. These data are also potentially important because they can cover significant portions of coastal ocean model domains. They make it possible, for the first time, to track the location and movement of

mesoscale ocean features in a fashion analogous to the superior capabilities provided by data inputs to numerical weather forecast models. In addition, HF radar systems are all-weather. They are not affected by clouds or changing ocean conditions.

Many questions still exist, however, about the details and effectiveness of HF radar-derived surface currents as sources for data assimilation. On one level, data descriptors needed to define the requisite error covariance functions are not yet well known. Errors in HF radar-derived currents arise from a variety of sources, including electromagnetic interference, ships, and poorly constrained inversion algorithms. Some insight into these errors can be obtained comparing with data from in situ moored current meters or drifting buoys, but the true nature of the errors and the best models for describing them are likely to come from algorithm simulations such as the work of Laws et al. (2001). An even bigger challenge is presented by the need to relate surface-only data to the three-dimensional model variables. Given perfect surface velocity data, this issue still exists. Mechanisms for the surface-to-depth information exchange are a focus of this study as well as earlier studies described below (e.g., Oke et al., 2002).

This paper has the following structure: Section 2 describes the ICON hydrodynamic model set up along with previous work related to assimilation of HF radar-derived surface velocities and the general hypothesis adopted here that these data are best used as corrections to surface wind forcing. Section 3 presents Empirical Orthogonal Function (EOF) descriptions of the sub-tidal variability in the HF radar-derived currents and in model-generated currents using two different wind forcing products. The particular data assimilation approaches used here are described in section 4, while results from the different assimilation schemes are presented in Section 5 based on comparisons with independent, sub-surface velocity observations from two mooring sites. Finally, discussions and conclusions are presented in Section 6.

2. Modeling Background

2.1 ICON hydrodynamic model

The numerical model used in this study was developed within the framework of the ICON project. It is a fine-resolution ocean model covering Monterey Bay and the adjacent coastal

areas (Shulman et al. 2002, 2000). The model has an orthogonal, curvilinear grid, extending 110 km offshore and 165 km in the alongshore direction (Fig. 1). The horizontal resolution is 1-4 km, with the maximum resolution in the Monterey Bay vicinity. Vertically, the model is characterized by a realistic bottom topography with 30 vertical sigma levels. The ICON model code is a three-dimensional, free surface implementation based on the Princeton Ocean Model (POM; Blumberg and Mellor, 1987). On the open boundaries, it is coupled to a larger-scale model of the Pacific West Coast (PWC, Clancy, et al., 1996, Rochford and Shulman, 2000), which is also based on POM.

Atmospheric forcing of the ICON model, or any high resolution coastal model, is a critical component of the simulations. The ICOM model has been run using a variety of forcing and boundary conditions (Shulman et al. 2002). In terms of the wind stress forcing, two primary atmospheric products have been used: the operational Navy model called NOGAPS (Navy Operational Global Atmospheric Prediction System), which has a horizontal resolution of, approximately, 91 km and a nested, high-resolution, non-hydrostatic Navy model known as COAMPS (Navy Coupled Ocean and Atmospheric Mesoscale Prediction System; Hodur, 1997), which was run in a re-analysis mode with horizontal resolution of 9 km in the region surrounding central California, including the ICON model domain. In the next section, we present evidence that the dominant sources of variability (synoptic storm systems) manifest similarly in the two atmospheric models. However, detailed analyses reveal that the improved resolution and dynamics of the COAMPS model lead to more structure in the wind field near shore, particularly near headlands and in locations, such as Monterey Bay, with strong sea breeze signals (Kindle et al., 2003). The higher resolution wind forcing also leads to increased variability in the modeled ocean temperatures and currents, particularly in the vicinity of the major upwelling centers that exist north and south of Monterey Bay (Blencoe, 2001).

2.2 Data Assimilation Approaches

There are many choices and degrees of freedom involved with the adjustment of model-predicted variables based on observations. As was mentioned above, the choices related to assimilation of HF radar-derived currents fall into two categories, although they need not be mutually exclusive. First one must choose a particular minimization scheme, including specification of error

covariance functions. This step is often influenced by the limits of available computing resources and, as in the case of HF radar-derived currents, by minimal or non-existent error models. The second step involves the projection of the surface-only observations onto the three-dimensional model variables. If three-dimensional covariance functions are available, these two steps become one.

A recent study by Oke et al. (2002) combined the two steps described above into one procedure. They used a well-known data assimilation scheme known as Physical-space Statistical Analysis System (PSAS; Cohn et al., 1998). For their error model, they developed statistical correlations between surface velocity and subsurface velocity, temperature, and salinity in order to derive three-dimensional model corrections based on the surface-only HF radar data. In that case, three-dimensional, non-homogeneous and non-isotropic estimates of forecast error covariances among prognostic model variables were used in the PSAS-based data assimilation scheme. The three-dimensional, non-homogeneous and non-isotropic forecast error covariances were derived from an ensemble of 18 typical summer model simulations.

The successful data assimilation experiments conducted by Oke et al. (2002), modeled the coastal ocean over the Oregon Continental Shelf with maximum depths around 300 m. With the narrow shelf along central California, our similarly sized, Monterey Bay area domain includes full-ocean depths exceeding 3000 m. It is not expected that variability below the surface layer in the Monterey Bay model necessarily correlates with surface velocities. In addition, for operationally configured coastal models, which are forced with atmospheric products that are variable in time and space and coupled on open boundaries to larger-scale models, the estimation of three-dimensional, forecast error covariances using an ensemble of typical simulations, represents a very challenging problem. For these reasons, we did not attempt to reproduce the results obtained by Oke et al. (2002) using the ICON model.

Alternative methods exist to project surface information into the subsurface model domain using physical principles rather than statistical covariances (see, for example, Haines, 1991; Shulman and Smedstad, 1998). With this in mind, the general approach that we followed in this study, and the precursors to it, was to relate HF radar-derived surface velocities to corrections in the

model wind forcing. Given the depths measured by HF radar (0.5–1.5 m), this conceptual link to the interfacial momentum transfer appears even more reasonable.

Lewis et al. (1998), attempted the first HF radar-based wind corrections in a model of Monterey Bay. In that study, a pseudo-shearing wind stress was added to the stress due to wind forcing. This pseudo-shearing stress depended on the differences between model-predicted velocities and HF radar-derived velocities and had the form:

$$\tau_{pw} = \rho C_d \left(\mathbf{u}^{\mathbf{o}} - \mathbf{u}^{\mathbf{m}}\right)\left|\left(\mathbf{u}^{\mathbf{o}} - \mathbf{u}^{\mathbf{m}}\right)\right| \quad (1)$$

where τ_{pw} is pseudo-wind stress, ρ is the water density, C_d is an unknown drag coefficient, $\mathbf{u}^{o}$ are HF radar-derived surface currents and $\mathbf{u}^{m}$ are model-predicted surface currents. In Lewis et al. (1998), τ_{pw} was added to the wind stress; the resulting net surface stress was then used to force the ocean model. The unknown drag coefficient, C_d, was determined from a special optimization problem that minimized the norm of the stress τ_{pw}. The application of (1) should improve the agreement between model and HF radar currents, as was demonstrated in Lewis et al. (1998). However, the specification of C_d represents a significant challenge to this approach. The method chosen makes no use of (or provision for) a priori knowledge of error covariances that could better define the optimal blending of model-predicted and observed surface currents. Furthermore, wind forcing was corrected only at model locations that were within the HF radar footprint, which can introduce unrealistic irregularities at the edges of that footprint.

With the development of the nested ICON model, Shulman et al. (2000) implemented the PSAS scheme and began initial assimilation experiments using the data-based velocity covariance functions described below. In that study, corrections were made only to the model's surface currents. In the present study we followed a two-step approach: 1) corrections to model-predicted surface currents were computed from the HF radar-derived surface currents using the PSAS scheme and the monthly varying error covariance functions described below and 2) those corrections were projected below the first model bin using two different methods based on physical arguments related to energy conservation or Ekman-type momentum transfer. Results from the different projection schemes were compared against the no-assimilation baseline as well

as the no-projection case of Shulman et al. (2000) using independent velocity profiles measured at two mooring sites.

3. Statistical Descriptions.

Before any data assimilation experiments were run with the ICON model, we investigated the dominant modes of variability in the wind-forced model currents alongside similar calculations performed with the HF radar-derived currents. The intention here was not to produce an exhaustive investigation of the processes contained in the model output or in the data, but rather to verify that the dominant processes were similar in each representation of the coastal velocity field. (Data assimilation should not be expected to adjust the output of a model that does not intrinsically simulate the features of interest.)

Below we present an EOF analysis of HF radar-derived surface currents as well as ICON model surface currents. Spatial EOF modes for HF radar surface currents in 1999 were computed using a scalar technique. That is, north-south velocity component grids were added to the array containing east-west velocity component grids, and a single variance decomposition was performed. Following that, the two halves of the given spatial modes were combined to represent the vector flow at each grid point. Parallel EOF computations were made for surface velocity fields from the subset of ICON model grid locations that most closely matched the HF radar data grid. In the case of the model output, results from two separate runs were used: one forced by the NOGAPS wind product, which has a spatial resolution of 91 km, and another forced with output from the high-resolution (9 km), non-hydrostatic COAMPS atmospheric model. The ICON model does not have tides, so HF radar data were 33 hr low-pass-filtered before the EOF decomposition was made.

Results from the EOF analyses are shown in Figure 2 in terms of the percentage of variance explained by the first ten spatial velocity modes. Remarkably, the variance partitioning is nearly identical for the observed velocity fields and the two different model runs. The first modes account for about 50% of the variance and the second modes account for about 15% of the variance. In all cases, at least 80% of the subtidal velocity variance is accounted for by the first

five modes. The spatial patterns for modes 1 and 2 are shown in Figure 3. They too are quite similar between the observations and model runs, particularly for the dominant mode. The conclusion here is that the dominant variability in Monterey Bay is related to the alongshore flow across the mouth of the bay, which is slightly more jet-like in the observations. In this case, there is very little difference between the two model runs, indicating that spatial wind resolution is not a primary factor in the alongshore flow pattern, although it is still possible that wind structures that are not resolved by the 9 km COAMPS fields account for the relatively narrow jet in the observations.

The amplitude time series for the mode 1 patterns exhibit reversals that correlate with reversals (or relaxations) in the dominant alongshore, upwelling-favoring wind forcing. The mode 1 amplitude time series for the observation grid is shown in Figure 4, together with the amplitude of the alongshore wind component at the M1 mooring near the center of Monterey Bay. The event-to-event correspondence is clear, particularly during the spring and summer upwelling seasons. The scatter illustrates the significant regression. Similar results were found for the model-based mode 1 amplitudes compared with the alongshore wind component. No significant correlation was found between mode 1 amplitudes and cross-shore wind, or between either wind component and any of the mode 2 amplitudes. The mode 2 amplitudes do indicate, however, a predominance of negative events or counterclockwise flow around Monterey Bay, which is consistent with the direct observations.

The patterns exhibited in Mode 2 differ more noticeably between the observations and the model results. In all cases, the flow is related to a single circulation cell. The model patterns exhibit more closed circulation within Monterey Bay, particularly in the case of the high-resolution wind forcing. It is important to remember, however, that these modes are empirical and that modes 2 through 4 contain similar amounts of variance. The true closed circulation pattern often observed in Monterey Bay (e.g., Paduan and Rosenfeld, 1996) is likely represented by a combination of these modes.

The statistical results here show that, at the surface, the dominant modes of variability are captured by the model fields. Closer comparisons with moored and shipboard observations and

satellite imagery (Shulman et al., 2000, 2002; Blencoe, 2001) suggest that the model also produces realistic features, including: 1) mesoscale filaments and eddies associated with upwelling-favoring wind events, 2) a meandering, alongshore ocean front between the upwelled water and the warmer water of the California Current, and 3) two narrow poleward-flowing boundary currents associated with the California Undercurrent and the shallow Inshore Countercurrent. Also, the model does well in reproducing the mean water temperatures and salinities at a given depth, and shows a high correlation between observed and model temperatures for different levels (Shulman et al., 2002). The model demonstrates a good agreement between observed and model-predicted mixed layer depths at moorings M1 and M2 (See Table 1).

Table 1. Observed and model-predicted mixed layer depths (MLD).

	M1		**M2**	
ΔT Threshold	**0.1°C**	**0.2°C**	**0.1°C**	**0.2°C**
Observed MLD (m)	11.0	11.7	14.8	16.6
ICON Model MLD (m)	11.6	12.3	14.2	16.5

However, the comparisons between observations and model results show that, even with high-resolution atmospheric forcing, the model captures the "essence" but not the "details" of the observed variability. For example, in many instances, there is lag (in space and time) between observed and model-predicted features. In section 5, we present two-dimensional maps of complex correlation (according to Kundu, 1976) between model-predicted and observed ADCP currents. These correlations show that the moorings were positioned close to the boundary between high and low correlation between model and observations. This suggests a shift in space and time between model and observed features. We can speculate many reasons for this: inaccuracies in bathymetry, atmospheric forcing, etc. However, the assimilation of observations usually helped to minimize the lag between model predictions and observations.

4. Data Assimilation Approach.

As we stated in the Introduction, the following two-step data assimilation scheme is considered in this study:

1. Corrections to the model-predicted surface velocity were estimated using the PSAS scheme from the differences between the model forecast and HF radar-derived surface currents.
2. Corrections to surface velocities derived in step 1 were related to corrections in model wind forcing based on physical principles, such as conservation of energy or Ekman theory. This introduces an instantaneous subsurface projection of the surface velocity corrections derived in step 1.

In the following sub section, the first step of the approach is described.

4.1 Estimation of analysis (updated) field of surface currents.

Here, we briefly describe the approach used for estimation of the analysis field of the model surface currents. The analysis (updated) field of the model surface currents is derived from:

$$\mathbf{U}_s^a = \mathbf{U}_s^f + K\left(\mathbf{U}_s^o - H\mathbf{U}_s^f\right), \tag{2}$$

where $\mathbf{U}_s{}^a$ are the analyzed surface currents, $\mathbf{U}_s^f$ are model forecast surface currents, and $\mathbf{U}_s{}^o$ are HF radar-derived surface currents. H is the interpolation operator, and the matrix K is the Kalman gain, which depends on the forecast error covariance matrix, P^f, and the observation error covariance matrix, R:

$$K = P^f H^T \left(HP^f H^T + R\right).^{-1} \tag{3}$$

The PSAS algorithm first solves a linear system with unknown quantity $\mathbf{q}$ such that:

$$\left(HP^f H^T + R\right)\mathbf{q} = \mathbf{U}_s^o - H\mathbf{U}_s^f \tag{4}$$

and then the analyzed state $\mathbf{U}_s{}^a$ is obtained from the equation:

$$\mathbf{U}_s^a = \mathbf{U}_s^f + P^f H^T \mathbf{q}. \tag{5}$$

In the numerical experiments described in this study, covariance matrices P^f and R were derived from the estimates of horizontal covariances of the observed HF surface current data.

Estimates of the horizontal covariance for HF radar surface velocities were done month-by-month for each month in the record containing at least two weeks of reasonably full velocity maps. The long-term results were fairly consistent with velocity decorrelation scales on the order of 5-10 km. The east-west velocity component, U, tended to have slightly longer cross-shore scales, while the north-south component, V, had slightly longer scales in the alongshore direction. It was found that the derived covariances for surface currents could be fit and explained assuming the streamfunction $C_{\phi\phi}$ depends only on the distances between points in x and y directions. This leads to a covariance matrix that is a rotated Gaussian function with scales of different length in the x and y directions. To illustrate, let us consider the Gaussian function:

$$\mathrm{cov}_{i,j} = a\exp\left\{-\left[\left(\left(\xi_i - \xi_j\right)/R_1\right)^2 + \left(\left(\zeta_i - \zeta_j\right)/R_2\right)^2\right]\right\}, \qquad (6)$$

where (i,j) are two locations with coordinates (ξ_i,ζ_i) and (ξ_j,ζ_j) and ξ,ζ is an orthogonal coordinate system; the amplitude, a, and length scales, R_1 and R_2, are unknown parameters. Suppose that $C_{\phi\phi}$ can be represented by (6) when axis ξ is the physical axis x rotated counterclockwise with the angle θ. Using Helmholtz's theorem and assuming that the flow is completely nondivergent (geostrophic), the covariance functions for velocity components (C_{uu} and C_{vv}) can be easily derived (see Daley, 1991). These covariance functions depend on four unknown parameters (a,R_1,R_2 and θ), which can be determined from the best fit to the observed covariances. The results of the best fit show that the surface velocity covariances have a weak seasonal cycle, with the orientation of the major axis changing slightly throughout the year. Sample spatial covariance functions are shown in Figure 5 for April 1999 together with the best-fit parameters for the entire year. In the preliminary data assimilation experiments described below, these modeled covariance functions are used for the forecast error covariance matrix, P^f. The observation error covariance matrix, R, is given by a diagonal matrix with normalized values.

4.2 Subsurface projection of the corrections to the model surface velocity.

According to Equation (2), the corrections for the model surface velocities are: $\delta\mathbf{U}_s = \mathbf{U}_s^a - \mathbf{U}_s^f = \left(\delta u_s, \delta v_s\right)$. In Shulman et al. (2000), these corrections were applied to the surface

layer of the model; as a result, the ICON model predictions were improved in comparison to the model predictions without HF radar data assimilation. In this case, corrections to surface velocities were projected into the ICON model subsurface fields based only on the model's governing dynamics.

Below, we propose alternate schemes for instantaneous projection of velocity corrections into the subsurface. It is supposed that $\delta \boldsymbol{U}^s$ are due to errors in the wind forcing of the model and that related physical principles can be used to accomplish the projection. Below, we employ principles based on: 1) conservation of energy and 2) Ekman theory.

4.2.1 Energy conservation.

Corrections $\delta \boldsymbol{U}^s$ to the surface model velocities will change the model energy balance. This change of energy due to the work performed by wind stress relative to surface velocity corrections will have the form:

$$\delta E = \int_S \boldsymbol{\tau} \bullet \mathbf{U}_s ds. \tag{6}$$

In order to make HF radar data assimilation balanced in the sense of conservation of the model energy, we introduce the correction to the model wind forcing $\delta \boldsymbol{\tau}$. According to (6), and dropping the second-order terms, we have the following energy conserving equation for determining $\delta \boldsymbol{\tau}$:

$$\int_S \delta \boldsymbol{\tau} \bullet \mathbf{U}_s ds = -\delta E, \tag{7}$$

where, $\boldsymbol{U}^s$ is the surface model velocity without corrections.

It is clear that there are many distributions of $\delta \boldsymbol{\tau}$ that satisfy (7). We choose one that has a minimal norm but satisfies the energy balance (7). Considering (7) as a weak constraint, $\delta \boldsymbol{\tau}$ can be derived from the following minimization problem:

$$\min_{\delta \tau} J = \frac{\int_S \delta \boldsymbol{\tau} \bullet \delta \boldsymbol{\tau} ds}{\int_S \boldsymbol{\tau} \bullet \boldsymbol{\tau} ds} + \frac{\left(\int_S \delta \boldsymbol{\tau} \bullet \mathbf{U}_s ds + \delta E \right)^2}{\left(\int_S \boldsymbol{\tau} \bullet \mathbf{U}_s ds \right)^2}. \tag{8}$$

The solution to the minimization problem (8) has the following form:

$$\delta\boldsymbol{\tau} = \lambda \mathbf{U}_s, \tag{9}$$

where the Lagrange multiplier λ is given by:

$$\lambda = -\frac{\delta E}{\int_S \mathbf{U}_s \bullet \mathbf{U}_s ds} \frac{1}{\left(1 + cor^2\right)}$$
$$cor^2 = \frac{\left(\int_S \boldsymbol{\tau} \bullet \mathbf{U}_s ds\right)^2}{\int_S \mathbf{U}_s \bullet \mathbf{U}_s ds \int_S \boldsymbol{\tau} \bullet \boldsymbol{\tau} ds}. \tag{10}$$

By providing the minimum of (8), the corrections to wind stress $\delta\boldsymbol{\tau}$ derived from (9)-(10) will conserve the model energy and have the minimal norm among all possible corrections to wind stress, conserving the model energy. In section 5, the results of assimilation of HF radar surface currents with the conservation of the model energy will be presented.

4.2.2 Projection based on application of Ekman theory.

If the PSAS-based correction, $\delta\boldsymbol{U}^s$, to the surface model velocity is interpreted as a requirement to adjust the surface wind stress, then Ekman theory (Ekman, 1905) can be applied to estimate this additional wind stress, $\delta\boldsymbol{\tau}$, which has the following form:

$$\delta\tau_x = \rho\sqrt{\frac{A_v f}{2}}\left(\delta u_s - \delta v_s\right) \tag{11}$$

$$\delta\tau_y = \rho\sqrt{\frac{A_v f}{2}}\left(\delta u_s + \delta v_s\right), \tag{12}$$

where A_v is the eddy viscosity, f is twice the vertical component of the Earth's rotation vector. According to (11)-(12), the additional wind stress will produce Ekman transport, $\boldsymbol{M} = (M_x, M_y)$:

$$M_x = \rho\sqrt{\frac{A_v}{2f}}\left(\delta u_s + \delta v_s\right) \tag{13}$$

$$M_y = \rho\sqrt{\frac{A_v}{2f}}\left(\delta v_s - \delta u_s\right). \tag{14}$$

Note, that the Ekman transport (13)-(14) from additional wind stress (11)-(12) depends on the value of eddy viscosity (in contrast to the general Ekman theory). This is due to the fact that additional wind stress is actually estimated from knowing corrections to the *surface velocity,*

$\delta \boldsymbol{U}^s$. In the classical application, the integrated velocity field is specified by the *surface wind stress*.

Using Equations (11), (12) and Ekman theory, we can estimate corrections to subsurface velocity driven by the additional wind stress (11)-(12). The subsurface corrections, $\delta \boldsymbol{U}(z) = (\delta u(z), \delta v(z))$, have the following form:

$$\delta u(z) = \exp(-z/D_e)\left[\delta u_s \cos(-z/D_e) - \delta v_s \sin(-z/D_e)\right] \tag{15}$$

$$\delta v(z) = \exp(-z/D_e)\left[\delta u_s \sin(-z/D_e) + \delta v_s \cos(-z/D_e)\right] \tag{16}$$

where,

$$D_e = \sqrt{\frac{2A_v}{f}} \tag{17}$$

is Ekman depth.

The ICON model has 30 sigma levels σ_k, k=1,30 in the vertical, and subsurface velocities are defined in the middle of each sigma layer. This gives 29 vertical sigma locations for velocities. Subsurface velocity corrections are derived according to (15)-(16) by transforming z into the sigma coordinate system. In this case, the transport (estimated by numerical integration of these corrections over the water column) will be different from the Ekman transport $\boldsymbol{M}$ estimated according to (13)-(14). Moreover, the estimated transport from the subsurface corrections (15)-(16) will depend on the total depth of water column since the thickness of a sigma layer depends on depth at particular location.

In order to conserve the Ekman transport, the following scheme of subsurface projection is proposed. Let Mx_k and My_k be transports in the x and y directions, respectively, determined analytically by integration of (15)-(16) between σ_k and σ_{k+1} levels. The corrections to subsurface velocity are determined at the middle of kth layer (at $\sigma = (\sigma_k + \sigma_{k+1})/2$) from the following relations:

$$\delta u_k = \frac{Mx_k}{(\sigma_k - \sigma_{k+1})H} \tag{18}$$

$$\delta v_k = \frac{My_k}{(\sigma_k - \sigma_{k+1})H}. \tag{19}$$

In this case, the transport estimated by integration of corrections (18)-(19) over the water column will be equal to the corresponding Ekman transport (13)-(14). Details of the Ekman spiral, such as the location of the turning point, decay scale, and shape, are not conserved by (18)-(19).

To estimate errors introduced by the projections, we compared Ekman transports and Ekman spirals corresponding to (15)-(16) and (18)-(19). We varied the total depth H, values of $\delta \boldsymbol{U}^s$, and Ekman depth D_e while keeping the ICON vertical distribution of sigma levels. The results of these experiments show that projection (15) -(16) produces a maximum error in Ekman transport around 5% in the deeper areas (500-1000m). Significantly less error (down to 0.05%) is produced in shallow water because sigma coordinates of the model have a high vertical resolution near the surface in those regions. At the same time, the projection (18)-(19) gives errors of up to 50% in the depth of the Ekman spiral turning point, especially in deeper water (>500 m). Because of the topography within the ICON model domain, the absolute values of surface velocity corrections $\delta \boldsymbol{U}^s$, derived from PSAS, decrease significantly away from the HF radar footprint. Therefore, the errors associated with (15)-(16) to conserve Ekman transport, or (18)-(19) to conserve the shape of the Ekman spiral, will diminish away from the HF radar footprint.

Estimates of Ekman transport in the California Current system were reported by Chereskin (1995). Estimates of D_e and A_v were made in a number of different locations and conditions and yielded values ranging from 25m to 48m for Ekman depths and 0.0274 to 0.1011 m^2/s for corresponding viscosities. In this study, a constant (throughout the model domain) value of eddy viscosity A_v was used. In Section 5, the choice of this value and the corresponding value of D_e are discussed.

5. Data assimilation experiments.

Table 2 introduces short notations for the data assimilation schemes proposed in Lewis et al. (1998), Shulman et al. (2000), and schemes described in the previous section. Below, a comparison of these schemes' performance is presented using data from the summer period of 1999 (from June 1 to August 29) and August-September of 2000. In 1999, two ICON model control runs were used. The first was a model run forced with a 12-hourly NOGAPS wind (91km resolution); the second was a model run forced with a 12-hourly COAMPS wind (9km resolution). This enables us to evaluate the impact of the data assimilation on the ICON model predictions forced with different resolution wind products. In 2000, only one control model run was considered: the ICON model was forced with 12-hourly, 9km resolution COAMPS wind and heat fluxes.

Table 2. Descriptions of and designations for assimilation schemes.

Scheme	Designation
Assimilation of CODAR data according to the additional wind stress (1) (the scheme outlined in Lewis et al. (1998))	Lewis98
Assimilation of CODAR data only into the surface layer of the ICON model (Shulman et. al. (2000))	DA00
Assimilation of CODAR data into the surface layer of the ICON model and with subsurface projection based on the energy conservation principle (Section 5.2.1)	DA00ENG
Assimilation of CODAR data into the surface layer and vertical projection based on Ekman theory, equations (15) -(16)	DA00Ek1
Assimilation of CODAR data into the surface layer and vertical projection based on Ekman theory, equations (18) -(19)	DA00Ek2

The ICON model does not have tides; for this reason, the HF radar data were 33-h low-pass filtered, and spatial and temporal data gaps were filled, in accordance with the automated procedure for filling and filtering the data described in Paduan et al., 2001. Hourly HF radar-derived surface currents maps were used; therefore, the analysis (updated) field of the model surface currents (see Section 4.1) was estimated each hour.

For the 1999 study period, the ICON model current predictions with and without assimilation of HF radar data were compared to currents measured by a 300 kHz RD Instruments Acoustic Doppler Current Profiler (ADCP) mounted in a downward-looking configuration on the

Monterey Bay Aquarium Research Institute's (MBARI) surface mooring at 122.40° W, 36.67° N, designated M2. For the three months of data used here (June 1 - Aug. 29, 1999), the ADCP was set up to measure in 4-m depth bins and generally returned good data in the depth range from 6 to 120 m. For the 2000 study period, the ICON model current predictions with and without assimilation of HF radar data were compared to currents measured at M2 and at another surface mooring at 122.02° W, 36.74° N, designated M1. (For summer of 1999, ADCP data at M1 were unavailable.) In 2000, the M1 and M2 ADCPs were set up to measure in 8-m depth bins, with the first bin at 15.58m for M1 and 12.5 m at M2.

The HF radar footprints and location of the M1 and M2 stations are shown on Fig. 6. The comparisons at M1 illustrate the impact of HF radar data assimilation on the ICON model predictions inside the HF radar footprint; however, comparisons at M2 illustrate the influence of HF radar assimilation on the model predictions in an area outside, but within a decorrelation length from, available observations.

The magnitudes of complex correlation coefficients and angular displacements between the ADCP and ICON model currents were used for evaluating the various data assimilation schemes. The magnitude ρ of the complex correlation coefficient between the ADCP and ICON model currents for a particular depth was estimated by using the following formula (Kundu, 1976):

$$\rho = \sqrt{\mathrm{Re}^2 + \mathrm{Im}^2} \tag{20}$$

where,

$$\mathrm{Re} = \frac{\sum_t \left(u_t^o u_t^m + v_t^o v_t^m \right)}{\sqrt{\sum_t \left(\left(u_t^o \right)^2 + \left(v_t^o \right)^2 \right) \sum_t \left(\left(u_t^m \right)^2 + \left(v_t^m \right)^2 \right)}}$$

$$\mathrm{Im} = \frac{\sum_t \left(u_t^o u_t^m - v_t^o v_t^m \right)}{\sqrt{\sum_t \left(\left(u_t^o \right)^2 + \left(v_t^o \right)^2 \right) \sum_t \left(\left(u_t^m \right)^2 + \left(v_t^m \right)^2 \right)}}$$

u_t^m, v_t^m and u_t^o, v_t^o are de-meaned model and observed east-west and north-south components of velocity. The angular displacement θ (phase angle, average veering) between the ADCP and ICON model currents for a particular depth was estimated as:

$$\theta = \tan^{-1} \frac{\sum_t \left(u_t^o v_t^m - v_t^o u_t^m \right)}{\sum_t \left(u_t^o u_t^m + v_t^o v_t^m \right)}. \tag{21}$$

The value of θ is only meaningful if ρ is significant. Standard statistical techniques (see, for example, Emery and Thomson, 1998) were used for estimating 95 % significance levels of the correlation. For the summer of 1999 experiments, the significant level was 0.207; for August-September of 2000, it was 0.261.

The magnitudes of complex correlation coefficients (20) were examined using a range of assimilation schemes and parameter values (see notations in Table 2). In all cases, the correlations were computed as a function of depth starting at the topmost ADCP bin. That shallowest observation depth was 5.8 m at M2 during the 1999 study period. During the 2000 study period, it was 12.5 m at M2 and 15.6 m at M1. By comparison, the shallowest model bin was everywhere less than 6 m. (In the deepest regions where the water depth is 3500 m, the thickness of the ICON model surface layer was only 3.5 m.) Therefore, all of the results depicted here represent depth bins below the actual surface layer where model-data comparisons were utilized by the various assimilation schemes.

Results using different values of Ekman depth in the projection schemes DA00Ek1 and DA00EK2 are shown in Figures 7 and 8 for cases from 1999 and 2000, respectively. Overall, both schemes exhibited similar correlations and the results were similar using different values of D_e, with slightly better results obtained for D_e = 46 m (A_v = 0.1 m^2/s). (The exception is the case with scheme DA00Ek2 in 1999 and NOGAPS wind forcing, which exhibited the greatest sensitivity to choice of D_e.) Note that the value of D_e = 46 m is in agreement with the estimate reported by Chereskin (1995) based on long-term current meter observations in the California Current system. Most important, all of the combinations of Ekman depth, projection scheme, and wind forcing show clear evidence of improvement compared with the no-assimilation cases.

For the conditions in 1999, the improvement extended down to the 120 m depth limit of the ADCP observations. For the conditions in 2000, however, the improvement was limited to the upper 70 m.

A further examination of the data assimilation sensitivities is presented in Figure 9, which shows the magnitudes of the complex correlation for different assimilation schemes as outlined in Table 2. The results indicate that assimilation of HF radar data according to the scheme Lew98 does not improve the model correlation with subsurface ADCP currents (Figure 9a). As was mentioned above, this may be explained by the fact that there is no instantaneous projection of surface information into the subsurface using this scheme. In addition, the corrections are based only on differences between model-predicted and HF radar-derived currents at individual observation locations and the wind stress corrections are applied only within the HF radar footprint. (The M2 location was just outside the HF radar footprint in the 1999 study period.)

In contrast to the Lew98 scheme, both the DA00 and DA00ENG schemes apply surface corrections throughout the model domain based PSAS. In this case, corrections at a particular location depend not only on velocity differences observed at that location, but also at all other locations as a function of the spatial error covariance model. The results in Figure 9 indicate that these PSAS-based schemes performed better than the Lew98 scheme. The results also show that there was almost no difference between the standard PSAS scheme (DA00) and the augmented scheme that preserved ICON model energy (DA00ENG).

In most cases, the greatest model improvement—as determined by the correlations with subsurface ADCP data—was achieved using the schemes that employed velocity projection based on Ekman theory (i.e., DA00Ek1 and DA00Ek2). In those schemes, PSAS-derived surface corrections instantaneously affect surface layer velocities down to depths that depend on the selected Ekman depth. Results shown earlier for this study—based on correlations with the independent ADCP data—indicate that there is only a modest sensitivity to the choice of Ekman depth for these schemes.

In addition to producing larger magnitudes of the complex correlation between model-predicted and observed currents, a successful assimilation scheme must also preserve, on average, directions of the observed currents as is indicated by low phase angles in the complex correlation results (Kundu, 1976). For the cases studied here, angular displacements between ICON model-predicted and observed currents were generally in the range of –30 degrees to +30 degrees with and without assimilation. One exception was the resulting phases for scheme DA00Ek2 below 80 m at M1 in 2000. At these depths, however, all model runs showed a low correlation magnitude with M1 ADCP observations in 2000, which makes conclusions about angular displacements impossible.

Angular displacements (phases) of the complex correlation results for the better-performing schemes (DA00Ek1 and DA00Ek2) are shown together with the magnitudes in Figure 10 for the 1999 study period. In this case, only results for D_e = 46 m are shown in order to highlight the impact of the assimilation schemes and wind forcing. Runs without assimilation exhibited different correlation magnitudes in the different wind forcing cases, while the corresponding runs with HF radar data assimilation had very similar correlation magnitudes. In all cases, the average angular displacements at all depths were very close to zero. This supports the idea that HF radar data assimilation acts as an effective correction to the model's wind forcing.

Finally, it is important to investigate the sensitivity of the correlation results based on single-point mooring observations to horizontal location, particularly in light of the strong horizontal heterogeneity that is known to exist within the ICON domain. Except for the HF radar-derived surface currents, the available observations do not span horizontal space. This limitation is not true for the model output, of course. Hence, an indication of the horizontal velocity structure can be seen by mapping correlation magnitudes between the currents observed at the mooring location and the modeled currents throughout the domain.

The spatial variations of correlation magnitudes are shown in Figure 11 for various model runs compared with observations at the M1 or M2 mooring locations. In each case, the complex correlation magnitudes between HF radar-derived surface currents and currents in the topmost ADCP bin are also shown. From these results, it is evident that M2 in particular was located at a

boundary between high and low correlation. Correlation magnitudes actually increase and peak northwest (offshore) of the mooring location for the no-assimilation model runs. Correlation magnitudes for the M2 versus HF radar-derived currents by contrast are maximum at and slightly east (inshore) of the mooring location. Maps of correlations for the model runs using the DA00Ek1 assimilation scheme show altered patterns with the maximum correlation region immediately east (inshore) of the mooring location in closer agreement with the HF radar-derived patterns. This altered and, presumably, improved pattern is present at all depths and in both the NOGAPS and COAMPS wind forcing cases. Because the M2 mooring was outside the HF radar footprint, the results presented illustrate the influence of HF radar data on model predictions outside the locations of the actual data.

The influence of HF radar data assimilation on the model predictions inside of the HF radar data footprint is illustrated on the lower panel in Figure 11, which shows the correlation magnitudes based on observations at the M1 mooring location. Again, the data assimilation acts to alter the correlation patterns to be more in keeping with those derived from the HF radar data, although the positive effects in this case are limited to the upper 60 m or so as was seen earlier in the correlation profiles.

6. Discussions and Conclusions.

Comparisons of the statistical properties of the HF radar data and the observed wind indicate a strong correlation between the dominant alongshore, upwelling-favorable wind forcing and HF radar-derived surface currents. Because inadequate wind stress forcing fields is probably a significant source of error in ocean circulation model solutions, the idea of using HF radar data to help correct surface wind forcing looks promising. In this paper, we evaluated the utility of HF radar data used in this fashion based on results from the ICON program around Monterey Bay.

Comparisons of the magnitudes of complex correlation between model and observed currents, down to 120 m, indicated that assimilation of HF radar data according to the pseudo-shearing wind stress scheme of Lewis et al. (1998) has very limited effect, particularly outside the

immediate HF radar data footprint. Improvement is seen, however, using schemes that employ a statistically based assimilation scheme to correct all model surface currents based on the field of HF radar-derived currents. In these applications, surface velocity corrections were developed based on the PSAS data assimilation scheme using error covariance functions modeled on monthly varying, observed velocity covariance functions. Two schemes were tested using PSAS-based assimilation acting only within the first model depth bin. The second one included the additional constraint of model kinetic energy conservation, although little difference was seen between these two schemes.

A greater impact of the data assimilation was seen when subsurface projection schemes were used. In this study, those schemes were based on a constant eddy viscosity, frictional boundary layer assumption (i.e., the classic Ekman theory). Although still ad hoc, particularly with regard to intrinsic assimilation time scales, it was argued that these schemes are consistent with the concept of improving or "nudging" the wind-driven momentum transfer based on the mismatch between model-predicted and HF radar-derived surface currents. Unlike alternative schemes that employ fully three-dimensional error covariance functions within the assimilation step, these schemes directly alter model velocities only within the near surface layer, which was within the upper 40 m for most of the cases examined in this study. The Ekman-based projection methods were seen to be robust in that they improved model performance in all cases, and to depths that extended below the depths at which velocity corrections were applied.

The Ekman-based schemes proposed and tested here do include the need to choose the precise shape of the velocity correction profile through the choice of Ekman depth (i.e., eddy viscosity) and the numerical projection algorithm applied in the presence of a model grid whose vertical resolution varies horizontally (e.g., a sigma-coordinate grid). The results presented here showed the Ekman-based projection schemes to be relatively insensitive to the various choices of Ekman depth and vertical integration algorithm. Furthermore, the Ekman depth that exhibited the best results (D_e = 46 m) was consistent with estimates by Chereskin (1995) from the same region based on long-term current meter observations.

As an additional check, complex correlation phases were investigated to be sure that data assimilation resulted in currents that were in the same direction, on average, as the observed currents, which was the case (Figure 10). The notion of phasing was further explored by investigating the horizontal variation of velocity correlation within the HF radar field and the model results as compared to the fixed mooring locations. Maps of correlation between model-predicted and ADCP currents showed that the M2 mooring was located in an area of intermediate correlation for model runs without assimilation (Figure 11). The highest correlated model currents were located northwest of the mooring in those runs, while the correlations between HF radar-derived currents and the near-surface ADCP bin at M2 were higher east of the mooring site. This indicates the presence of a spatial shift between modeled and observed features. It also points out potential problems involved with using single-point mooring observations to validate a three-dimensional circulation model. That is, relatively small spatial offsets in the modeled features can lead to an unrealistically poor assessment of model performance when data are compared only with model output from the mooring location.

In this study, data assimilation using HF radar-derived surface currents projected into the near-surface Ekman layer improved the correlations between modeled and observed currents down to depths of 70 m to 120 m at the mooring sites (Figures 7-10). The data assimilation also altered the spatial correlation patterns bringing them more in line with those based on the HF radar-derived currents (Figure 11). These results are encouraging, but they will become be more widely applicable and accepted given a dynamical mechanism for the improved model performance. Such an explanation is essential if it is to be argued that the methods used here should be exported to locations beyond Monterey Bay.

What are the possible explanations for altered model currents below the depths subjected to explicit corrections as part of the data assimilation scheme? It seems clear that one of two physical mechanisms is responsible for the fluid accelerations at depth: 1) friction driven by changed vertical shear conditions or 2) pressure gradients related to changed horizontal density gradients. In the first case, only the model's turbulence closure algorithm is available to mix momentum downward, which is an unlikely explanation for accelerations observed well below the mixed layer. The second mechanism is more likely to be responsible for the results seen in

this study. Horizontally variable corrections produce horizontally variable density anomalies. These, in turn, require geostrophic velocity adjustments over a finite depth range that is thicker or thinner depending on the background stratification. A very important aspect of this argument is the need for horizontally distributed velocity observations, such as those obtained from a network of HF radar sites. If the ground-truth data were obtained at only one location, or if the model-data mismatch were uniform at all locations, then the data assimilation approach taken here would be completely ineffective below the explicit correction layer (approximately one Ekman depth). An exception to this argument may be found at the model's coastal boundary. At those locations, any applied corrections may have a disproportionate effect on velocities at depth due to the rigid boundary conditions. (This is a potential problem that should be studied in more detail in future studies using this methodology.)

The deeper model velocities likely respond to the data assimilation technique used here through a type of Ekman pumping analogous to the forcing exerted by wind stress curl. According to (13)-(14), the assimilation technique produces a vertical velocity anomaly equal to:

$$W = \nabla \bullet \mathbf{M} = \sqrt{\frac{A_v}{2f}}\left(\nabla \bullet \delta \mathbf{U}_s + curl_z \delta \mathbf{U}_s\right). \tag{23}$$

This vertical velocity must be absorbed in the underlying fluid (i.e, below the Ekman layer), which can be presumed to have been in geostrophic balance. Therefore, horizontal current anomalies will be produced as the fluid adjusts to the new density field. An indication of this behavior using the results of this study is given in Figure 12, which shows a map of vertical velocity anomaly integrated over the entire 1999 study period ($\int W dt = \int \nabla \bullet \mathbf{M} dt$) for data assimilation scheme DA00Ek1 and the NOGAPS wind forcing. The coarse-resolution NOGAPS wind stress fields provided nearly zero wind stress curl forcing over the ICON model domain, while Ekman pumping due to the data assimilation provided a forcing field with small scales comparable to Monterey Bay. Enhanced model upwelling was forced in areas to the north and south of Monterey Bay, which are known upwelling sites (Rosenfeld et al., 1994). Within the Bay, another region of enhanced model upwelling was driven by the data assimilation scheme, which would have acted to strengthen cyclonic circulation in that area. Such a strengthening is consistent with the observation that more persistent cyclonic circulation was seen in the

Monterey Bay HF radar-derived currents than in the model currents without assimilation. We conclude from this that Ekman-based HF radar data assimilation can correct model currents in the mixed layer and seasonal thermocline by altering the pattern of upwelling.

As further evidence that we have identified the correct mechanism involved with accelerations at depth, we produced a proxy for the presumed horizontal changes in the model's density field. This was done by creating maps of the temperature anomaly at various depths between model runs with and without assimilation. Examples of the model temperature anomalies at 60 m are shown in Figure 13 for the initial phase of the 1999 study period. The data assimilation scheme produced clear anomaly patterns with cooler temperatures inside Monterey Bay and warmer temperatures outside at the 60 m. Initially, the anomalies were confined to the region of the HF radar data footprint, but the anomalies strengthened and expanded over the course of several days. A distinct, mesoscale warm anomaly developed early on just outside Monterey Bay at the edge of the HF radar footprint. That anomaly clearly propagated through the model domain toward the northwest over the course of about three weeks. Later in the study period, similarly sized temperature anomalies developed and propagated through the model domain. Hence, it is clear that the effects of assimilation of HF radar-derived currents, which took place only within the near-surface layer and in a geographically limited region, were felt at thermocline depths and at all locations in model. The results of this study showed that these effects improved model performance within and near to the region of HF radar data. However, more work must be done to understand the implications of this approach on model performance far from the data footprint, particularly in light of the way “disturbances” radiate away from the data region.

The relatively rapid time scale on which anomalies propagated through the model domain (days to weeks) may provide an explanation for the differences we observed between the 1999 and 2000 study periods. In the latter period, the data assimilation approach was less successful in terms of its depth of influence (model performance was improved only down to about 70 m as compared with 120 m during the 1999 period). Given the mechanism for vertical (and horizontal) propagation of information, the method used here can be expected to be sensitive to both the stratification and the initial mesoscale density structure. Although we did not impose an assimilation time scale beyond our initial sub-tidal filtering of the HF radar data, the model's

response must include an intrinsic time scale related to the geostrophic adjustment. For this reason, the method is likely to be more successful when the model-data mismatch fields contain patterns that persists for periods that are long compared with the adjustment time scale. In our example, this requires patterns to persist for periods of weeks rather than days. This is consistent with the situation in 1999 in which the model without assimilation failed to produce observed cyclonic circulation within Monterey Bay for a period of several weeks. By contrast, the model-data mismatch fields in 2000 exhibited much less consistent structures.

In the future, we will continue to focus on understanding the dynamic mechanisms by which surface velocity information impacts subsurface model currents. In parallel, we will continue to explore the sources of error in the HF radar data itself in order to improve error covariance models used in the first, PSAS phase of the data assimilation. Future model improvements should include tidal forcing and special handling of velocity assimilation near the coastal boundary. Despite this list of tasks remaining, it is clear that two-dimensional maps of surface currents from HF radar networks represent a useful and unique resource for the improvement of coastal ocean circulation models, particularly in the critical depth range encompassing the euphotic zone.

7. Acknowledgments

This work was supported by the National Ocean Partnership Program and by the Office of Naval Research (ONR) Ocean Modeling and Prediction Program under document numbers: N00014-98WR-30170, N00014-99WR-30118, N00014-00WR-20160, and N00014-02WR20086. I. Shulman was also supported by the Naval Research Laboratory's ONR program element 601153N. The authors wish to thank Drs. L. Rosenfeld and S. Ramp for many helpful discussions and J. Kindle and his group for providing open boundary data and atmospheric forcing for the ICON model. The efforts of R. Hodur produced the high-resolution COAMPS forcing fields. We would also like to acknowledge significant contributions from Dr. Chau-Ron Wu in initial development and testing of HF radar data assimilation methods while he was a post-doctoral research fellow of the University of Southern Mississippi (USM). B. Wilkinson of USM and M. Cook of the Naval Postgraduate School provided help with figure preparation and

computer time was provided by grants from the Department of Defense High Performance Computing Center at the U.S. Naval Oceanographic Office, Stennis Space Center, Mississippi. This manuscript is Naval Research Laboratory contribution number XXXX.

8. References

Barrick, D., 2003: Proliferation of SeaSonde coastal current-mapping radars. *Hydro International*, January/February 2003, 30-33.

Blencoe, D.G., 2001: Impact of high resolution wind fields on coastal ocean models. M.S. Thesis, Naval Postgraduate School, Monterey, CA, September, 71pp.

Blumberg, A., and G. L. Mellor, 1987: A description of a three-dimensional coastal ocean circulation model. In *Three Dimensional Coastal Models*, N.S. Heaps, Ed., Coastal and Estuarine Sciences, 4, Am. Geophys. Un., 1-16, 1987.

Chereskin T. K., 1995: Direct evidence for an Ekman balance in the California Current. *J. Geophys. Res*., **100**, 18261-18269.

Clancy, R.M., deWitt, P.W., May, P., Ko, D.-S., 1996. Implementation of a coastal ocean circulation model for the west coast of the United States, Proceedings of the American Meteorological Society Conference on Coastal Oceanic and Atmospheric Prediction, Atlanta, G.A., 72-75.

Cohn, S.E., da Silva, A., Jing Guo, Sienkiewicz, M., Lamich, D., 1998. Assessing the effects of data selection with the DAO Physical-space Statistical Analysis System. *Monthly Weather Revie*w, **126** (11), 2913-2926.

Emery, W. J. and R. E. Thomson, 1977: Data Analysis Methods in Physical Oceanography, Pergamon Press., 634 p.

Graber, H.C., B.K. Haus, R.D. Chapman, and L.K. Shay, 1997: HF radar comparisons with moored estimates of current speed and direction: Expected differences and implications. *J. Geophys. Res*., **102**, 18749-18766.

Haines, K., 1991: A direct method of assimilating sea surface height data into ocean models with adjustments to the deep circulation. *J. Phys. Oceanogr*., **21**, 843--868.

Hodur, R. M., 1997: The Naval Research Laboratory's Coupled Ocean/Atmosphere Mesoscale prediction System (COAMPS). *Monthly Weather Review*, **125**,1414-1430.

Kindle, J.C., R. Hodur, S. deRada, J. Paduan, L.K. Rosenfeld, and F. Chavez, 2003: A COAMPS™ reanalysis for the eastern Pacific: properties of the diurnal sea breeze along the central California coast. *Geophys. Res. Letters*, In Press.

Kohut,J., Glenn, S., and D. Barrick, 1999: SeaSonde is integral to coastal flow model development, *Hydro International*, **3**(3),32 -35.

Kundu, P. K., 1976: Ekman veering observed near the ocean bottom. *J. Phys. Oceanogr*., **6**, 238-242.

Laws, K. D.M. Fernandez, and J.D. Paduan, 2001: Simulation-Based Evaluations of HF Radar Ocean Current Algorithms. *J. Oceanic Engin*., **25**, 481-491.

Lewis, J.K, I. Shulman, and A.F. Blumberg, 1998: Assimilation of CODAR observations into ocean models. *Cont. Shelf Res*., **18**, 541-559.

Lipphardt, B. L., A. D. Kirwan, C. E. Grosch, J. K. Lewis and J. D. Paduan, 2000: Blending HF radar and model velocities in Monterey Bay through normal mode analysis. *J. Geophys. Res*., **105**, 3425-3450.

Oke, P. R., J. S. Allen, R. N. Miller, G. D. Egbert and P. M. Kosro, 2002: Assimilation of surface velocity data into a primitive equation coastal ocean model. *J. Geophys. Res*., **107**, 5-1 to 5-25.

Paduan, J. D., M. S. Cook, D. M. Fernandez, C. Whelan, I. Shulman and C.-R. Wu, 2001: Statistics and data assimilation results from long-term HF radar-derived surface currents around Monterey Bay, California. *Proceedings from 1st Radiowave Oceanography Workshop (ROW1)*, 7-9 April, 2001, Timberline Lodge, Mt. Hood, OR, Univ. of Miami Technical Report, 8pp, In Press.

Paduan, J. D., and M. S. Cook, 1997: Mapping surface currents in Monterey Bay with CODAR-type HF radar. *Oceanography*, **10**, 49-52.

Paduan, J.D., and H.C. Graber, 1997: Introduction to high frequency radar: Reality and myth. *Oceanography*, **10**, 36-39.

Paduan J.D., and L.K. Rosenfeld, 1996: Remotely sensed surface currents in Monterey Bay from shore-based HF radar (CODAR). *J. Geophys. Res.*, **101**, 20669-20686.

Paduan, J.D., L.K. Rosenfeld, S.R. Ramp, F. Chavez, C.S. Chiu, and C.A. Collins, 1999: Development and maintenance of the ICON observing system in Monterey Bay. *Proceedings, American Meteorological Society's Third Conference on Coastal Atmospheric and Oceanic Prediction and Processes*, New Orleans, LA, 3-5 November, pg. 226-231.

Rochford P. A. and Shulman, I., 2000. Boundary Conditions in the Pacific West Coast Princeton Ocean Model of CoBALT. NRL Technical Report, NRL/MR/7330-00-8245, 18 pp.

Rosenfeld, L.K., F.B. Schwing, N. Garfield, and D.E. Tracy, 1994: Bifurcated flow from an upwelling center: A cold water source for Monterey Bay. *Cont. Shelf Res*., **14**, 931-964.

Shulman I., C.-R. Wu, J.K. Lewis, J.D. Paduan, L.K. Rosenfeld, J.D. Kindle, S.R. Ramp, and C.A. Collins, 2002: High resolution modeling and data assimilation in the Monterey Bay area. *Cont. Shelf Res*., **22**, 1129-1151.

Shulman, I., Wu, C.-R., Lewis, J.K., Paduan, J.D., Rosenfeld, L.K., Ramp, S.R., Cook, M.S., Kindle, J.C., Ko, D.-S., 2000: Development of the High Resolution, Data Assimilating Numerical Model of the Monterey Bay. In Spaulding, M. L. and H. Lee Butler (Ed.), Estuarine and Coastal Modeling, pp. 980 - 994.

Shulman I., O. M. Smedstad, 1998: Data assimilation experiments with the Navy Layered Ocean Model. In Spaulding, M. L. and H. Lee Butler (Ed.), Estuarine and Coastal Modeling, 752- 765.

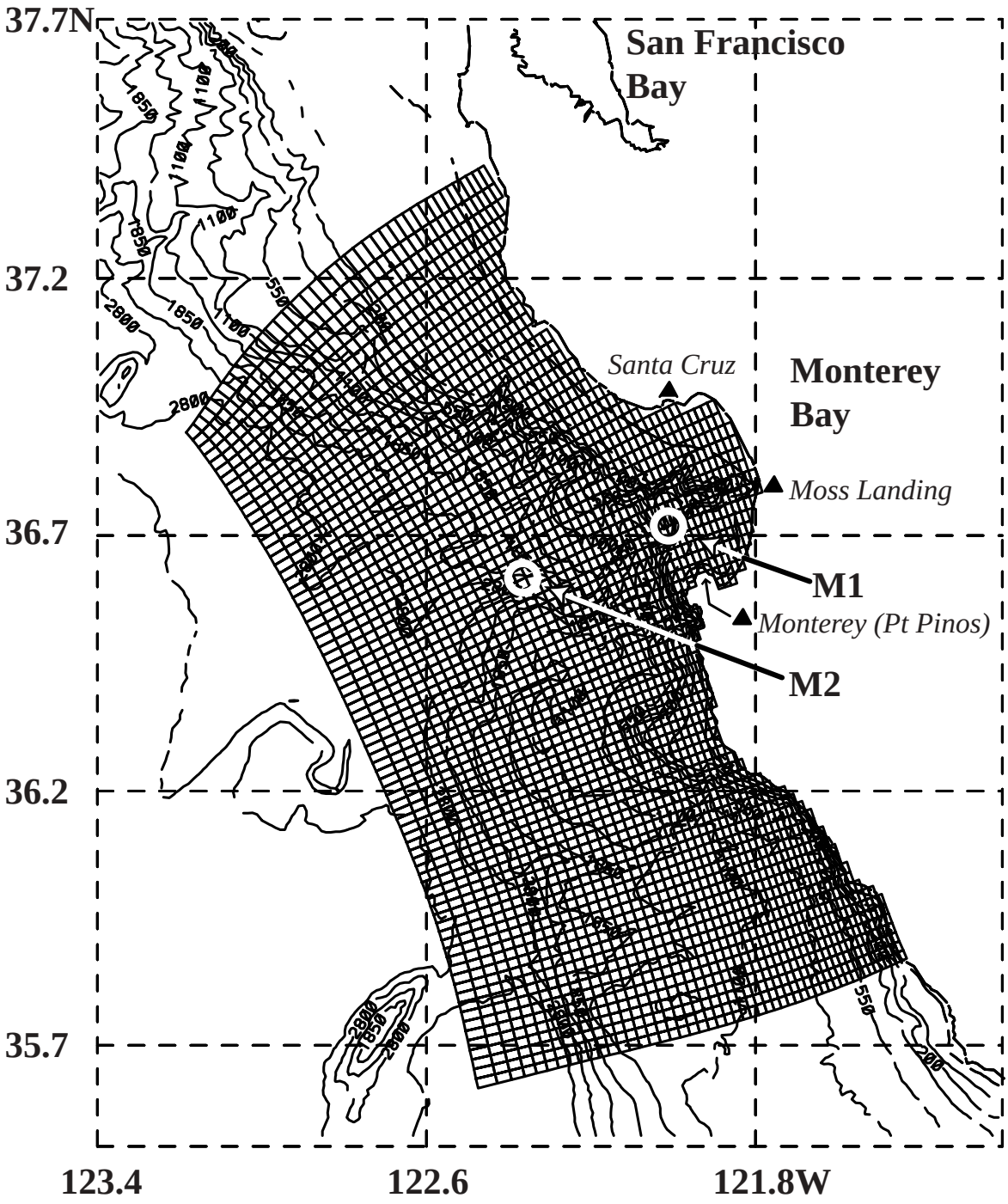

Figure 1. Model grid and bathymetry (m) with the locations of moorings M1 and M2 (circles) and the coastal HF radar sites (triangles).

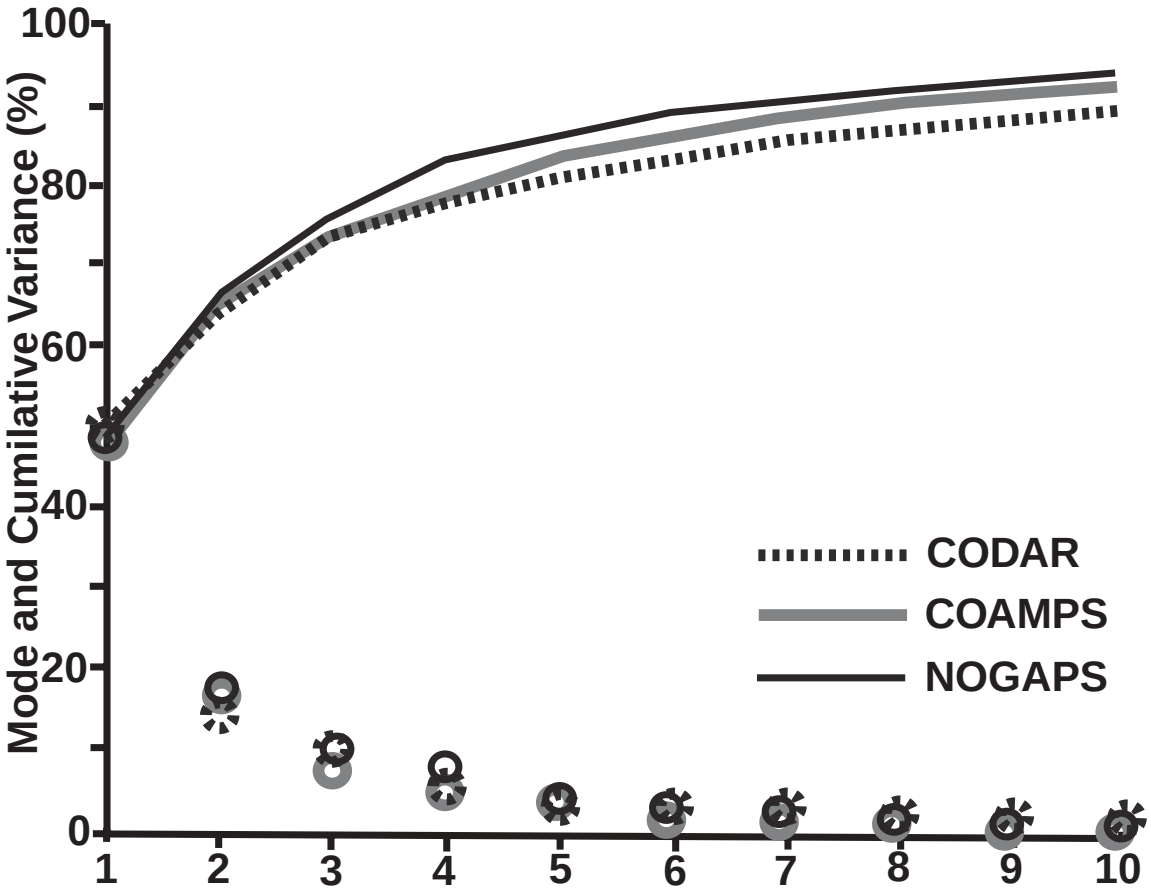

Figure 2. Percentage of variance explained in the spatial velocity modes for 1999 over the domain of the Monterey Bay HF radar coverage (symbols) together with the cumulative variance explained (lines). Results are shown for the radar-based observations (CODAR) and for numerical model runs using low resolution NOGAPS and high resolution COAMPS wind products.

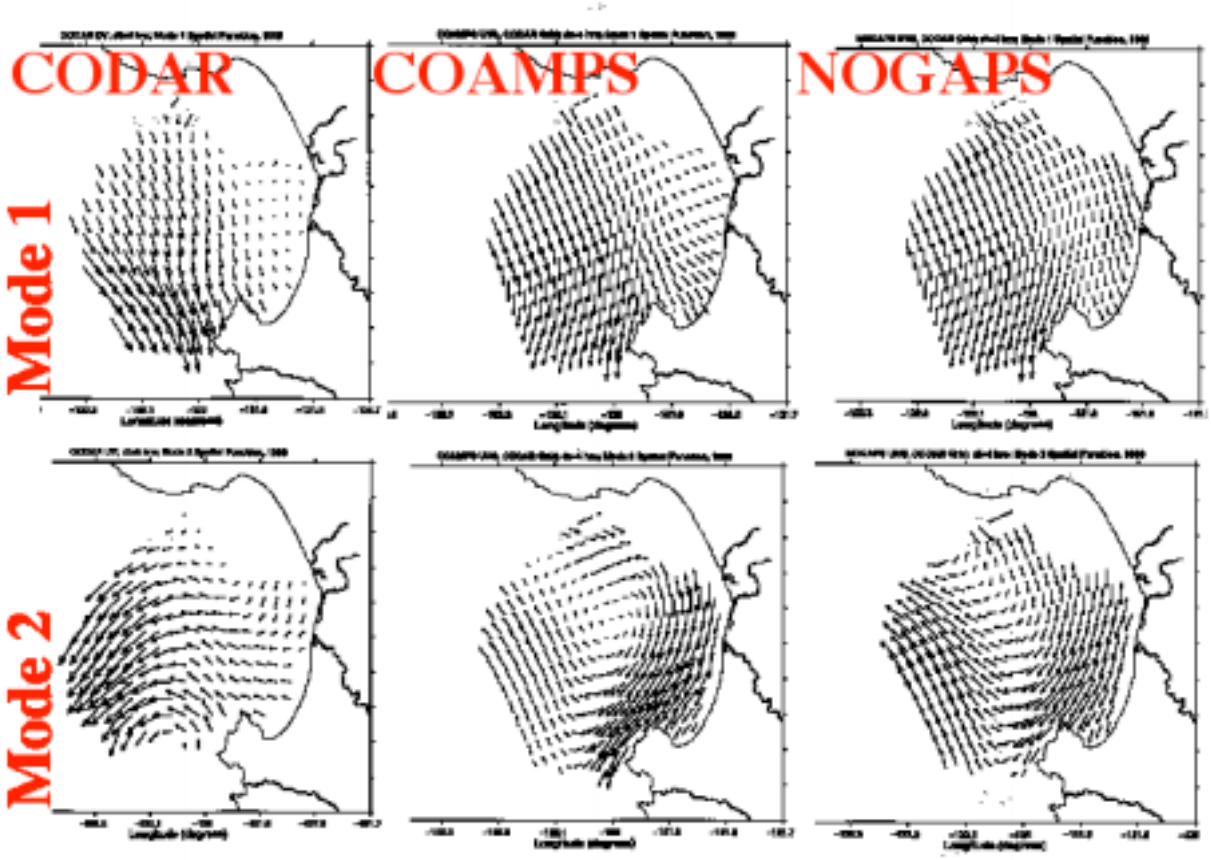

Figure 3. First and second spatial velocity modes for 1999 over the domain of the Monterey Bay HF radar coverage for the radar-based observations (CODAR) and for numerical model runs using low resolution NOGAPS and high resolution COAMPS wind products.

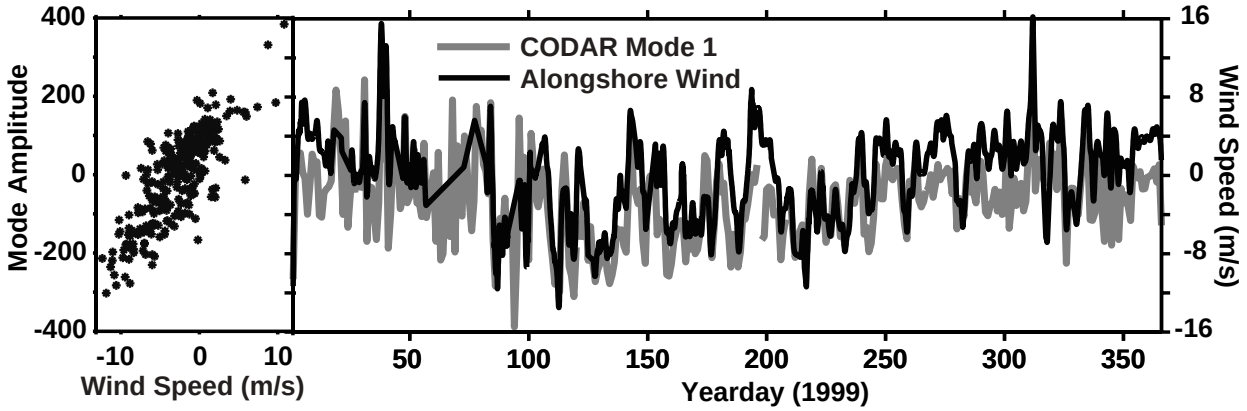

Figure 4. Alongshore component of wind at the M1 mooring and the mode 1 amplitude for the radar-derived (CODAR) surface velocity fields as a scatter plot (left panel) and versus time (right panel).

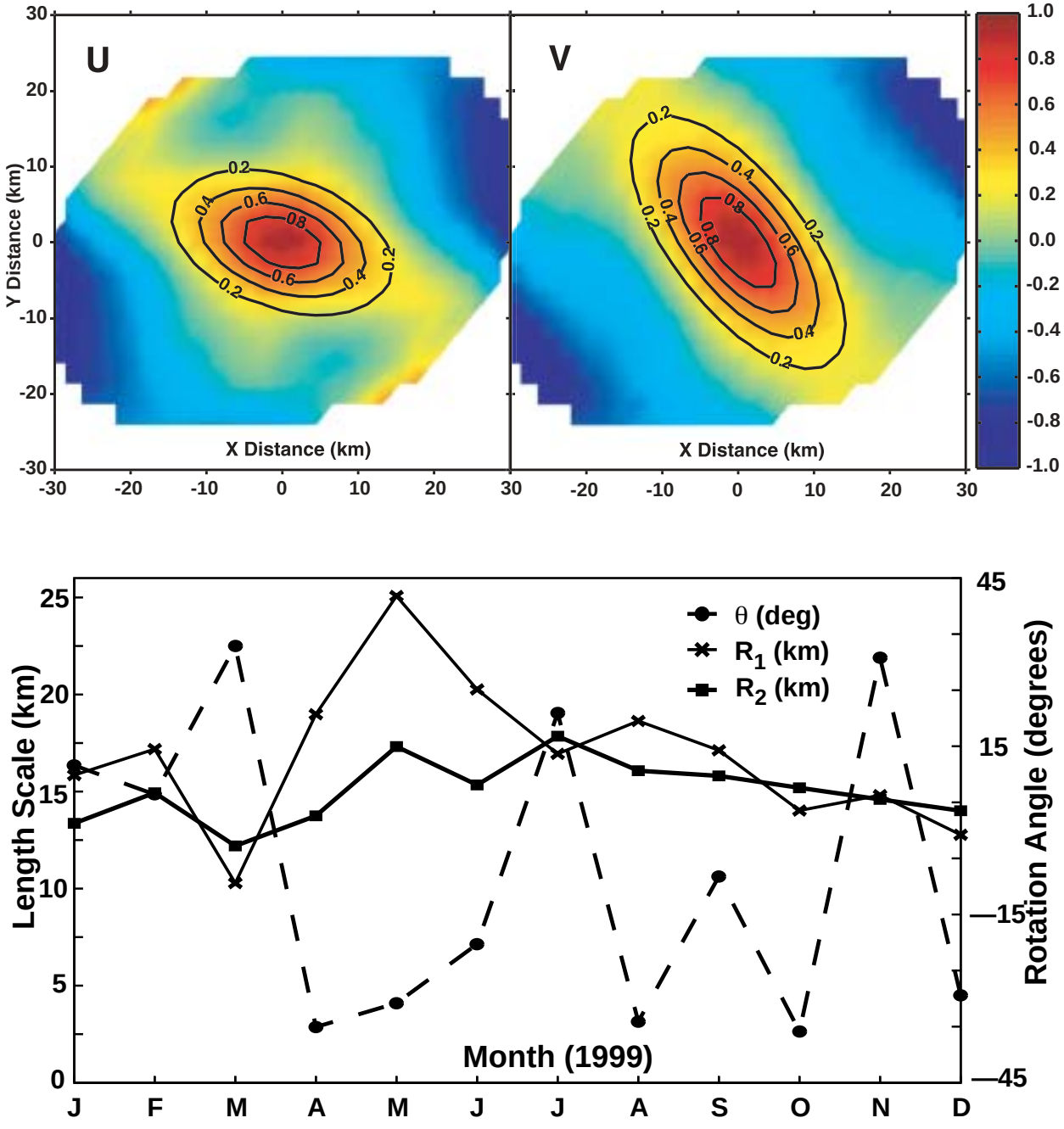

Figure 5. Normalized spatial separation covariances in April 1999 (upper) for east-west (U) and north-south (V) velocity components as observed (colors) and modeled using a two-dimensional Gaussian function (contour lines). Modeled covariance function parameters (Eqn-6; lower) computed monthly from the HF radar-derived surface velocities.

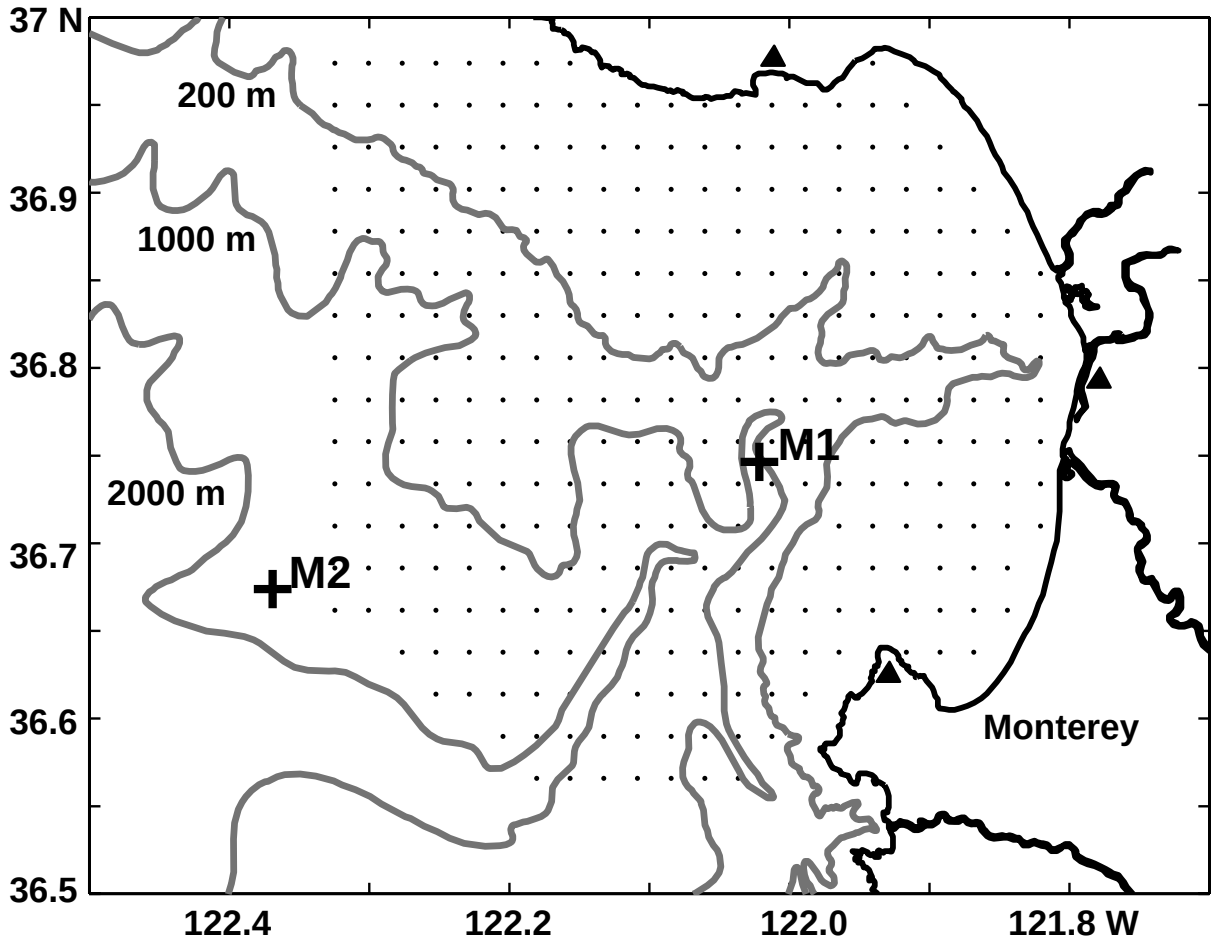

Figure 6. CODAR data footprints (dots) and locations of M1 and M2 moorings.

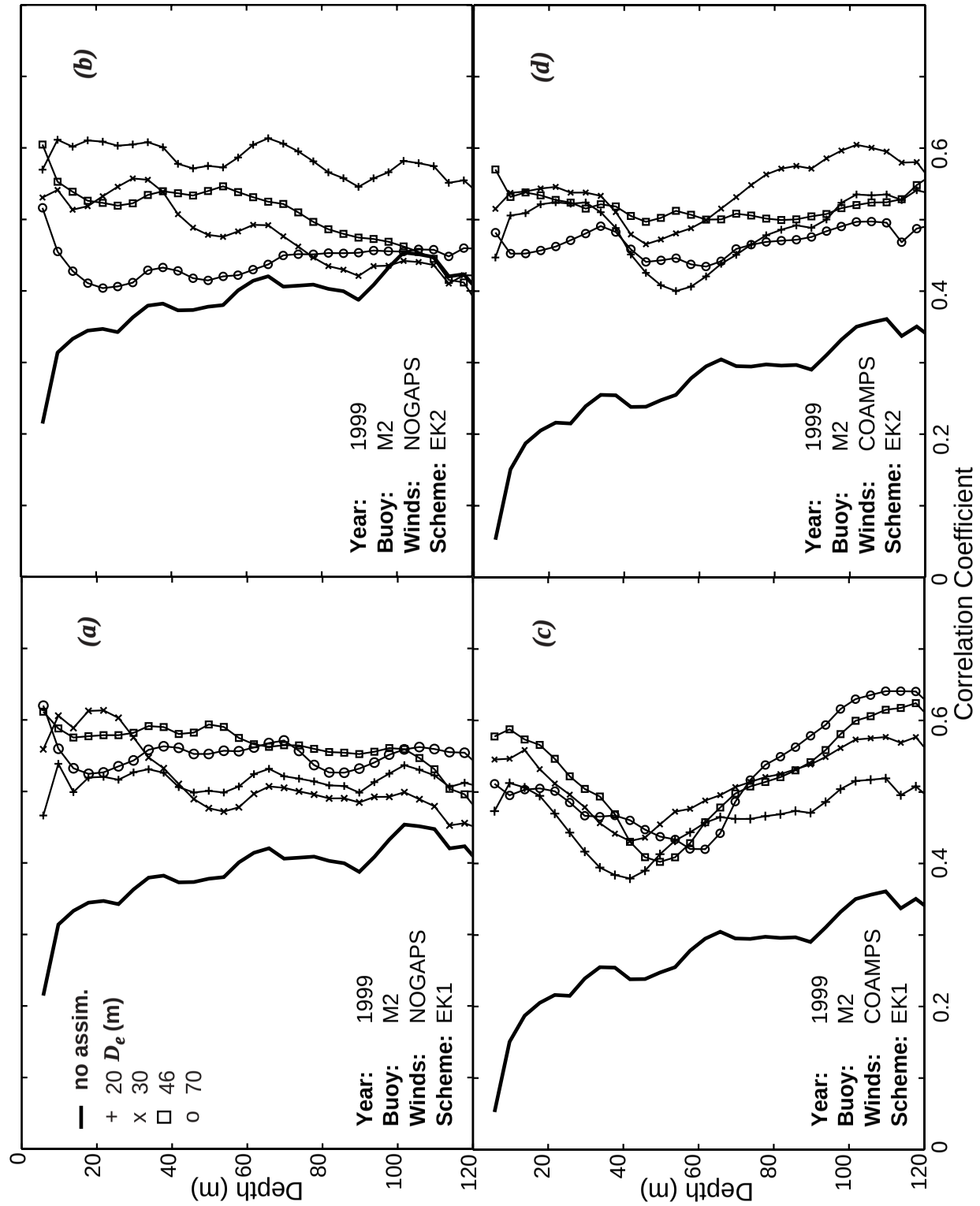

Figure 7. Magnitudes of the complex correlation between model-predicted currents and those observed at M2 in summer 1999 using various Ekman depths and NOGAPS forcing with schemes DA00Ek1 (a) and DA00Ek2 (b) or COAMPS forcing with schemes DA00Ek1 (c) and DA00Ek2 (d).

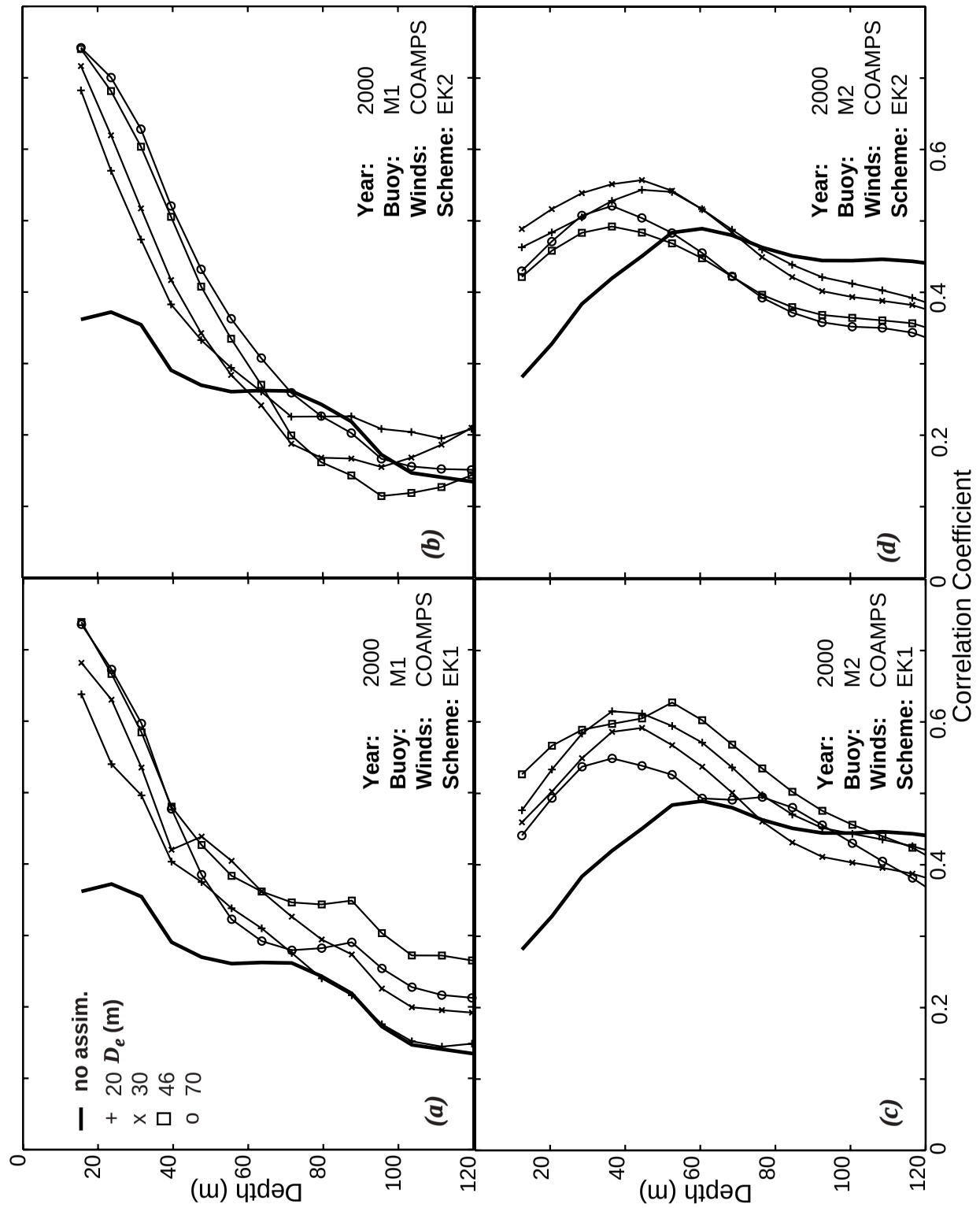

Figure 8. Magnitudes of the complex correlation between model-predicted currents and those observed in summer 2000 using various Ekman depths and COAMPS forcing with scheme DA00EK1 (a) or DA00Ek2 (b) at location M1 and DA00Ek1 (c) or DA00Ek2 (d) at location M2.

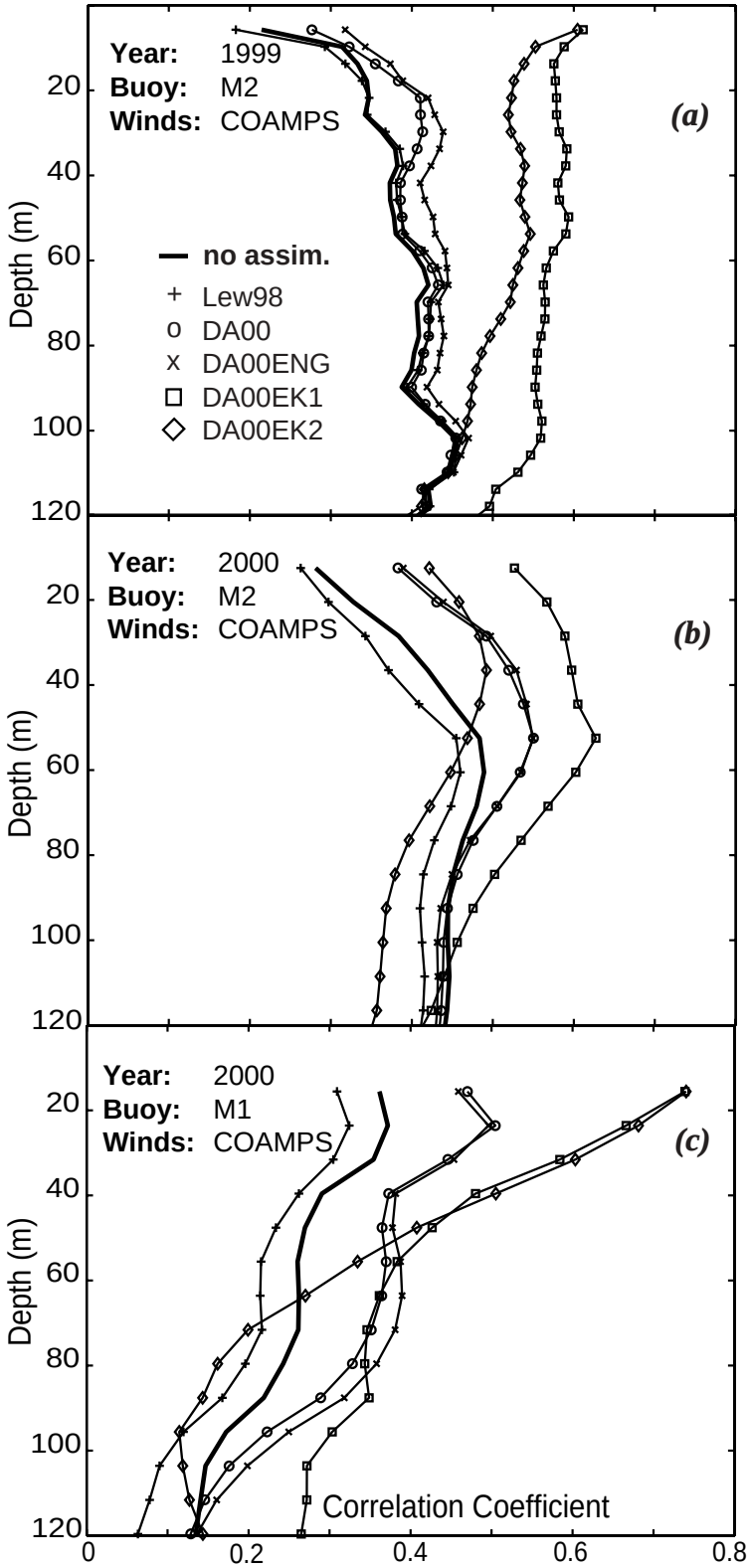

Figure 9. Magnitudes of the complex correlation between model-predicted currents and those observed for various assimilation schemes using COAMPS forcing and observations at M2 in 1999 (a) or 2000 (b) and M1 in 2000 (c).

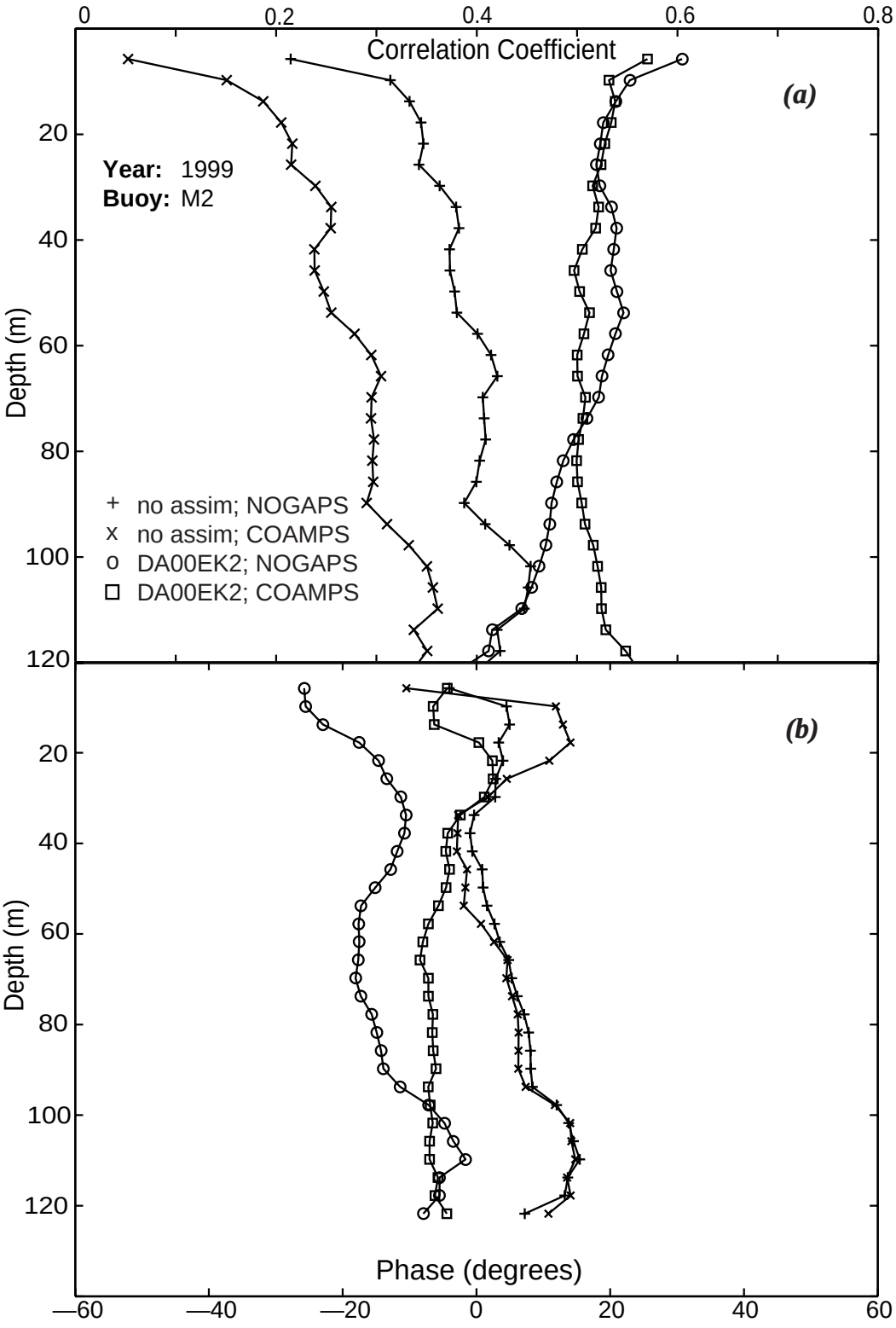

Figure 10. Magnitudes of the complex correlation (a) and phase (b) between model-predicted currents and those observed at M2 in 1999 for various assimilation schemes and wind forcing.

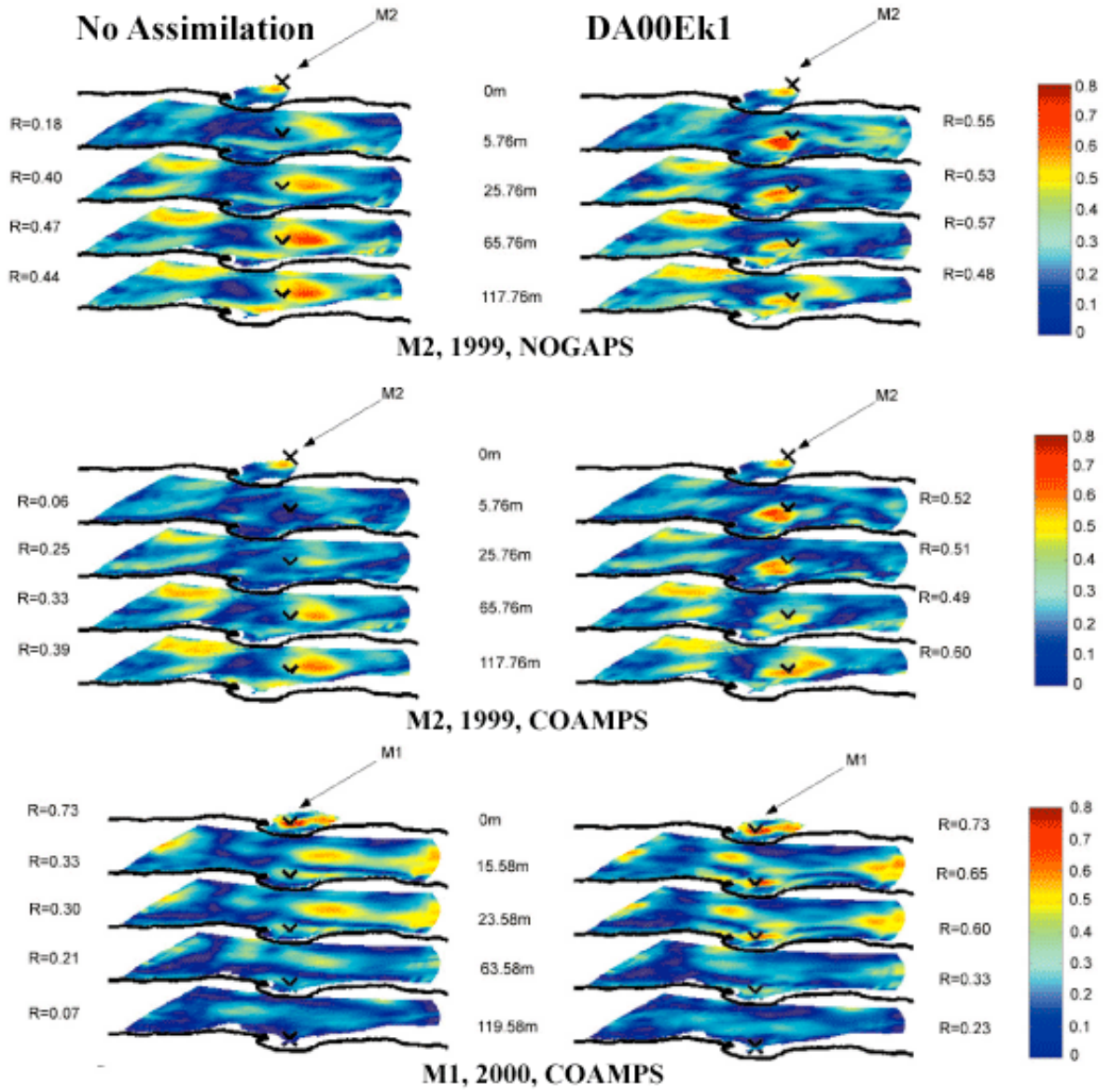

Figure 11. Maps of complex-correlation magnitudes between observed currents at the M1 or M2 mooring site and HF radar-derived surface currents (upper level in each panel) or model-predicted currents at various depths for 1999 using NOGAPS forcing (top) or COAMPS forcing (middle) and for 2000 using COAMPS forcing (bottom). In each case, results without data assimilation (left) and with data assimilation using the DA00Ek1 scheme (right) are shown.

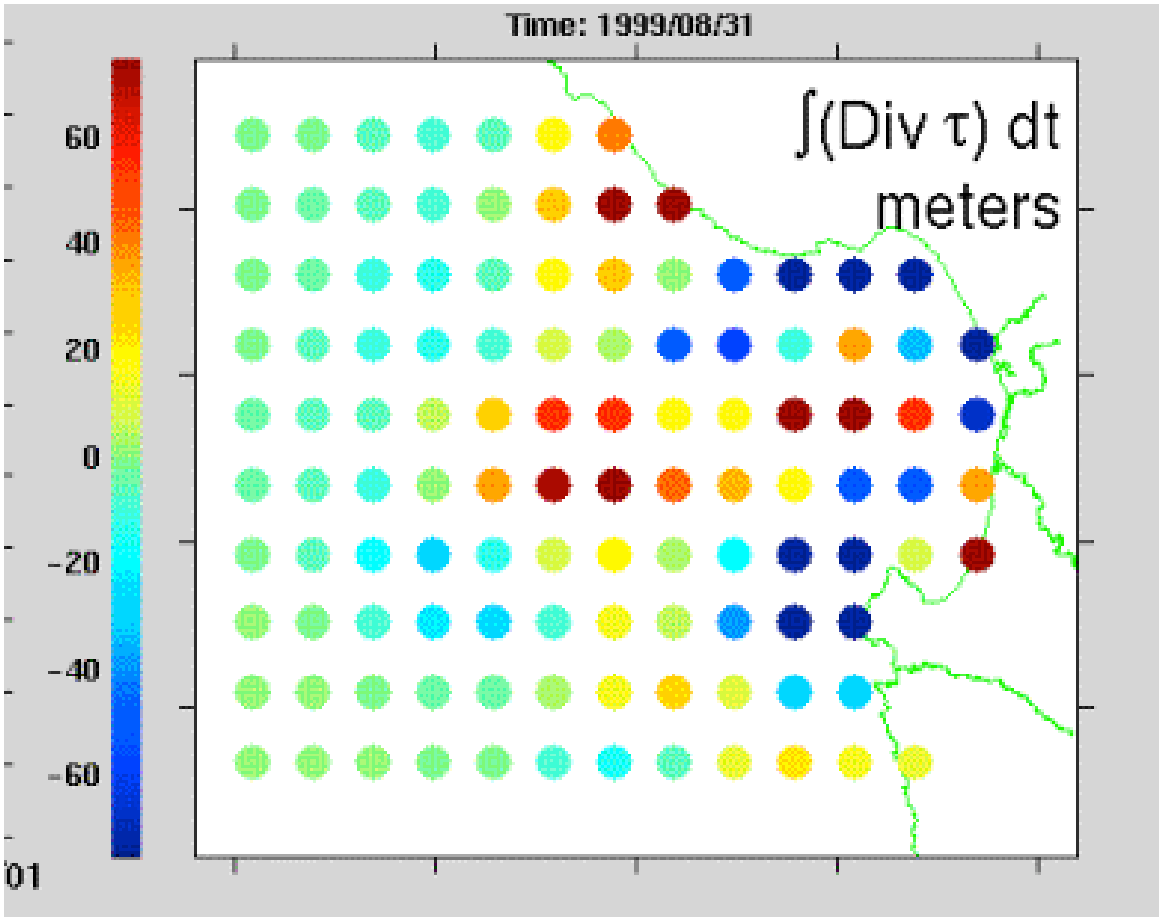

Figure 12. The map of Ekman pumping due to data assimilation (total over time) for the ICON model run with CODAR data assimilation according to scheme DA00Ek1.

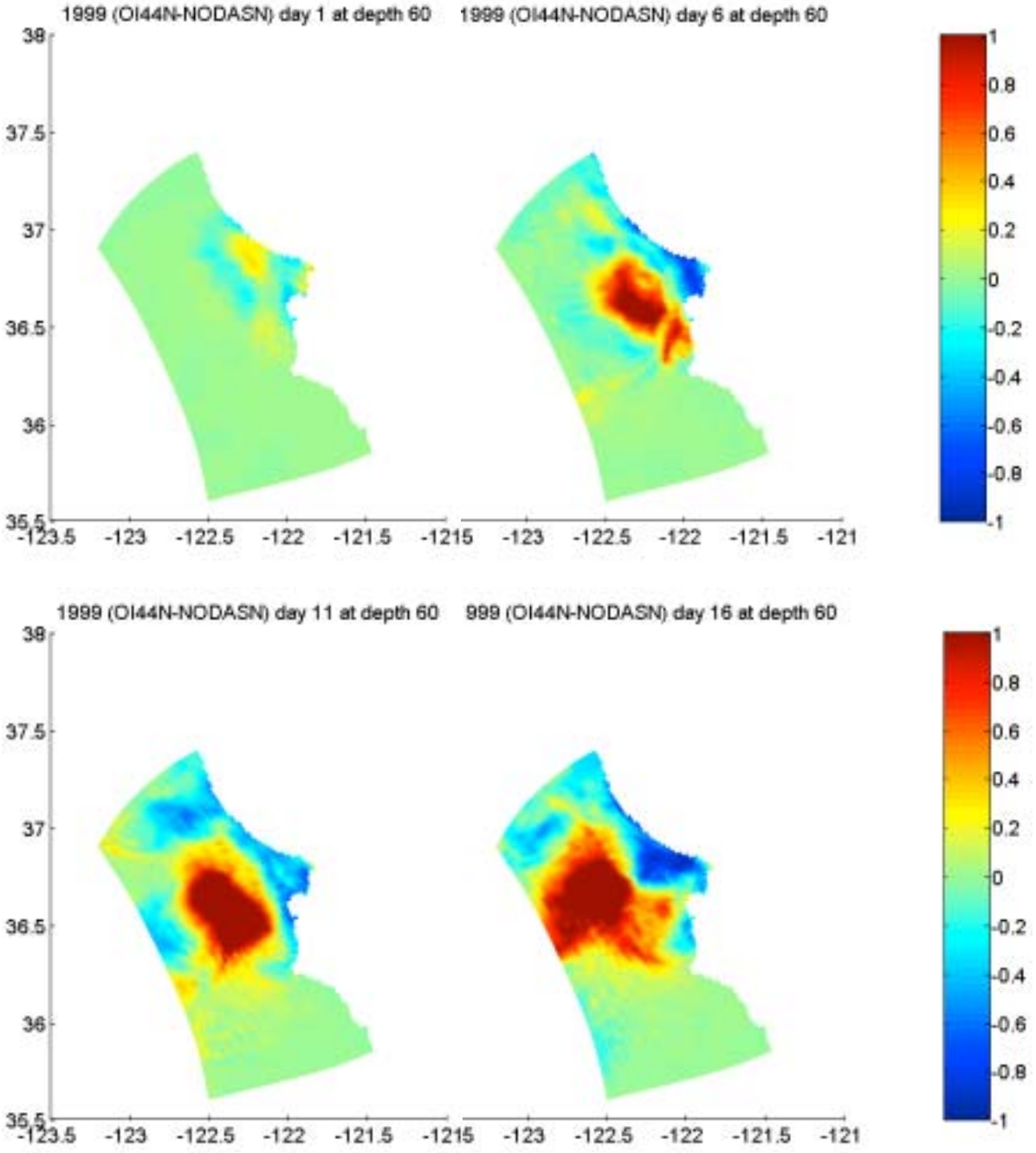

Figure 13. Temperature differences (degree C) at 60 m depth between ICON model runs with and without assimilation of HF radar-derived surface currents for days 1 (upper left), 6 (upper right), 11 (lower left), and 16 (lower right) during the 1999 study period using NOGAPS wind forcing and the DA00Ek1 assimilation scheme with D_e = 46 m.